

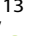











# Efficient generation of osteoclasts from human induced pluripotent stem cells and functional investigations of lethal *CLCN7*-related osteopetrosis

Uta Rössler,<sup>1,2,3</sup>  Anna Floriane Hennig,<sup>1,2,4,5</sup>  Nina Stelzer,<sup>1,2</sup> Shroddha Bose,<sup>6</sup> Johannes Kopp,<sup>1,2,4,7</sup>  Kent Søe,<sup>8,9,10</sup>  Lukas Cyganek,<sup>11,12</sup>  Giovanni Zifarelli,<sup>13</sup>  Salaheddine Ali,<sup>1,2,7</sup>  Maja von der Hagen,<sup>14</sup>  Elisabeth Tamara Strässler,<sup>15,16</sup>  Gabriele Hahn,<sup>17</sup> Michael Pusch,<sup>13</sup>  Tobias Stauber,<sup>6,18</sup>  Zsuzsanna Izsvák,<sup>19</sup>  Manfred Gossen,<sup>20,21</sup>  Harald Stachelscheid,<sup>22,23</sup>  and Uwe Kornak<sup>1,2,5,7</sup> 

<sup>1</sup>BIH Center for Regenerative Therapies (BCRT), Charité - Universitätsmedizin Berlin, corporate member of Freie Universität Berlin, Humboldt-Universität zu Berlin, and Berlin Institute of Health, Berlin, Germany

<sup>2</sup>Institute for Medical Genetics and Human Genetics, Charité - Universitätsmedizin Berlin, corporate member of Freie Universität Berlin, Humboldt-Universität zu Berlin, and Berlin Institute of Health, Berlin, Germany

<sup>3</sup>Berlin Institute of Health (BIH), Berlin, Germany

<sup>4</sup>Freie Universität Berlin, Berlin, Germany

<sup>5</sup>Institute of Human Genetics, University Medical Center Göttingen, Göttingen, Germany

<sup>6</sup>Institute of Chemistry and Biochemistry, Freie Universität Berlin, Berlin, Germany

<sup>7</sup>Max Planck Institute for Molecular Genetics, Berlin, Germany

<sup>8</sup>Clinical Cell Biology, Department of Pathology, Odense University Hospital, Odense C, Denmark

<sup>9</sup>Department of Clinical Research, University of Southern Denmark, Odense M, Denmark

<sup>10</sup>Department of Molecular Medicine, University of Southern Denmark, Odense M, Denmark

<sup>11</sup>Stem Cell Unit, Clinic for Cardiology and Pneumology, University Medical Center Göttingen, Göttingen, Germany

<sup>12</sup>German Center for Cardiovascular Research (DZHK), Partner Site Göttingen, Göttingen, Germany

<sup>13</sup>Istituto di Biofisica, CNR, Genoa, Italy

<sup>14</sup>Abteilung Neuropädiatrie, Medizinische Fakultät Carl Gustav Carus, Technische Universität Dresden, Dresden, Germany

<sup>15</sup>Department of Cardiology, Charité - Universitätsmedizin Berlin, Campus Benjamin Franklin, Berlin, Germany

<sup>16</sup>German Centre for Cardiovascular Research (DZHK), Partner Site Berlin, Berlin, Germany

<sup>17</sup>Institut und Poliklinik für Radiologische Diagnostik, Medizinische Fakultät Carl Gustav Carus Technische Universität Dresden, Dresden, Germany

<sup>18</sup>Department of Human Medicine, and Institute for Molecular Medicine, MSH Medical School Hamburg, Hamburg, Germany

<sup>19</sup>Max-Delbrück-Center for Molecular Medicine (MDC), Helmholtz Association, Berlin, Germany

<sup>20</sup>Berlin-Brandenburg Center for Regenerative Therapies, Charité Virchow Campus, Berlin, Germany

<sup>21</sup>Institute of Active Polymers, Helmholtz-Zentrum Hereon, Teltow, Germany

<sup>22</sup>Charité - Universitätsmedizin Berlin, corporate member of Freie Universität Berlin, Humboldt-Universität zu Berlin, and Berlin Institute of Health, Berlin, Germany

<sup>23</sup>Berlin Institute of Health (BIH), BIH Stem Cell Core Facility, Berlin, Germany

## ABSTRACT

Human induced pluripotent stem cells (hiPSCs) hold great potential for modeling human diseases and the development of innovative therapeutic approaches. Here, we report on a novel, simplified differentiation method for forming functional osteoclasts from hiPSCs. The three-step protocol starts with embryoid body formation, followed by hematopoietic specification, and finally osteoclast differentiation. We observed continuous production of monocyte-like cells over a period of up to 9 weeks, generating sufficient material for several osteoclast differentiations. The analysis of stage-specific gene and surface marker expression proved mesodermal priming, the presence of monocyte-like cells, and of terminally differentiated multinucleated osteoclasts, able to form resorption pits and trenches on bone and dentine *in vitro*. In comparison to peripheral blood mononuclear cell (PBMC)-derived osteoclasts hiPSC-derived osteoclasts

This is an open access article under the terms of the Creative Commons Attribution-NonCommercial-NoDerivs License, which permits use and distribution in any medium, provided the original work is properly cited, the use is non-commercial and no modifications or adaptations are made.

Received in original form September 9, 2020; revised form March 26, 2021; accepted April 21, 2021.

Address correspondence to: Uwe Kornak, MD PhD, and Anna Floriane Hennig, PhD, Institut für Humangenetik, University Medical Center Göttingen, Heinrich-Düker-Weg 12, 37073 Göttingen, Germany. Email: floriane.hennig@med.uni-goettingen.de

Additional Supporting Information may be found in the online version of this article.

Journal of Bone and Mineral Research, Vol. 36, No. 8, August 2021, pp 1621–1635.

DOI: 10.1002/jbmr.4322

© 2021 The Authors. *Journal of Bone and Mineral Research* published by Wiley Periodicals LLC on behalf of American Society for Bone and Mineral Research (ASBMR).

were larger and contained a higher number of nuclei. Detailed functional studies on the resorption behavior of hiPSC-osteoclasts indicated a trend towards forming more trenches than pits and an increase in pseudoresorption. We used hiPSCs from an autosomal recessive osteopetrosis (ARO) patient (BIHi002-A, ARO hiPSCs) with compound heterozygous missense mutations p.(G292E) and p.(R403Q) in *CLCN7*, coding for the  $\text{Cl}^-/\text{H}^+$ -exchanger CIC-7, for functional investigations. The patient's leading clinical feature was a brain malformation due to defective neuronal migration. Mutant CIC-7 displayed residual expression and retained lysosomal co-localization with OSTM1, the gene coding for the osteopetrosis-associated transmembrane protein 1, but only CIC-7 harboring the mutation p.(R403Q) gave strongly reduced ion currents. An increased autophagic flux in spite of unchanged lysosomal pH was evident in undifferentiated ARO hiPSCs. ARO hiPSC-derived osteoclasts showed an increased size compared to hiPSCs of healthy donors. They were not able to resorb bone, underlining a loss-of-function effect of the mutations. In summary, we developed a highly reproducible, straightforward hiPSC-osteoclast differentiation protocol. We demonstrated that osteoclasts differentiated from ARO hiPSCs can be used as a disease model for ARO and potentially also other osteoclast-related diseases. © 2021 The Authors. *Journal of Bone and Mineral Research* published by Wiley Periodicals LLC on behalf of American Society for Bone and Mineral Research (ASBMR).

**KEY WORDS:** *CLCN7*; hiPSCs; OSTEOCLASTS; OSTEOPETROSIS

## INTRODUCTION

Osteoclasts (OCs) are giant multinucleated cells formed by fusion of mononuclear precursors that differentiate from monocytes.<sup>(1)</sup> Although closely related to tissue macrophages, osteoclasts have a special capacity to resorb mineralized cartilage and bone, distinguishing them from all other phagocytosing cells. This resorption process crucially depends on extracellular acidification, which is required for dissolving the basic hydroxyapatite crystals deposited in the mineralized extracellular matrix.<sup>(2)</sup>

Genetic defects resulting in dysfunction of the components of this acid secretion mechanism partially or entirely block the resorption capacity, and lead to the accumulation of mineralized cartilage and bone with multiple consequences: (i) increased fracture rates; (ii) bone marrow insufficiency with anemia and immune deficiency; (iii) osteomyelitis; and (iv) blindness due to optic nerve damage.<sup>(1)</sup> Autosomal recessive osteopetrosis (ARO) is the most dramatic type of such defects, it is usually lethal during childhood. About 50% of the ARO cases are due to mutations in the T cell immune regulator gene 1 (*TCIRG1*, MIM #604592) encoding a subunit of the vacuolar proton pump. In 10% to 15% of ARO cases, biallelic mutations in the chloride channel 7 gene (*CLCN7*, MIM #602727) are responsible and in 2% to 5% mutations in the gene coding osteopetrosis-associated transmembrane protein 1 (*OSTM1*, MIM #607649). ARO is a rare disease, the incidence of all forms of ARO together is around 1:100,000. Mice deficient in *Ostm1* or *Cln7* show a neuronal lysosomal storage disease and a progressive deterioration of neurological function.<sup>(3–5)</sup> This is in line with the function of CIC-7 residing in lysosomes, where it regulates intraluminal ion homeostasis together with its  $\beta$ -subunit Ostm1.<sup>(6,7)</sup> A subset of patients with biallelic *CLCN7* loss-of-function mutations develops neurodegeneration, the so-called neuronopathic form of ARO. However, patients with *OSTM1*-ARO not only show neurodegeneration, but also cortical brain malformations, implying disturbed developmental processes.<sup>(8)</sup> Interestingly, also activating mutations in *CLCN7* can lead to abnormal brain development, albinism, and lysosomal storage without any bone phenotype.<sup>(9)</sup>

Human induced pluripotent stem cells (hiPSCs) with their capacity for unlimited self-renewal and differentiation into almost all cell types hold great potential for modeling human diseases and developing novel therapeutic approaches. Several protocols for differentiation of hiPSCs into macrophages and osteoclasts have been published, all of which rely on the formation of embryoid bodies for mesodermal specification and the induction of hematopoiesis.<sup>(10–15)</sup> However, the combination of cytokines, their concentrations, and the media

used vary between the existing protocols, which can have a strong impact on the outcome and costs of the experiments. Furthermore, the exact yield of hiPSC-osteoclasts and their characteristics have not been described in detail.

Here we report on a novel, robust osteoclast differentiation protocol with optimized media composition resulting in high osteoclast yield. We demonstrate comparable morphology and function of hiPSC-derived and primary peripheral blood mononuclear cell (PBMC)-derived osteoclasts. In addition, we successfully use our protocol to establish a disease model for ARO, using hiPSCs from a pediatric patient with biallelic *CLCN7* mutations and a lethal phenotype.

## MATERIALS AND METHODS

### Maintenance of hiPSCs

Osteoclast-related experiments were performed using hiPSC lines BIHi001-A and BIHi004-A (<https://hpscereg.eu/cell-line/BIHi001-A>, <https://hpscereg.eu/cell-line/BIHi004-A>, kindly provided by the BIH Core Facility Stem Cells), 10211.EURCC, UMGi014-C clone 14, and UMGi020-B clone 21 (isWT1.14 and isWT7.21 respectively, <https://hpscereg.eu/cell-line/UMGi014-C>, <https://hpscereg.eu/cell-line/UMGi020-B>, kindly provided by the UMG Stem Cell Unit) from control donors as well as osteopetrosis patient-derived cell lines BIHi002-A,<sup>(16)</sup> BIHi002-B, and BIHi002-C. Origins and reprogramming methods of the hiPSC lines are listed in Table S1. Methods and materials used for hiPSC reprogramming and characterization are further described in Supplementary Methods and shown in Table S11, Table S12 and Table S13. The hiPSCs were maintained in Essential 8 medium (Life Technologies, Bleiswijk, Netherlands) in Geltrex-coated (Life Technologies, Bleiswijk, Netherlands) 6-well dishes in a humidified normoxic incubator (37°C, 5% CO<sub>2</sub>) and routinely passaged in colonies at a ratio of ~1:20 every 4 to 5 days by using 0.5mM ethylenediamine tetraacetic acid (EDTA) (Life Technologies, Bleiswijk, Netherlands).

### Osteoclast differentiation of hiPSCs

At least 3 days before starting the differentiation, hiPSCs cultured in Essential 8 medium were adapted to mTeSR™1 (Stemcell Technologies, Vancouver, Canada) medium. For embryoid body (EB) formation and mesodermal induction, single cells were harvested by TrypLE Select Enzyme (Life Technologies, Bleiswijk, Netherlands) treatment. Subsequently,  $1.25 \times 10^4$  cells were seeded per well in a round bottom ultra-low attachment 96-well plate (Corning, Kennebunk, ME, USA) in 100  $\mu$ l mTeSR™1

medium supplemented with 50 ng/ml human bone morphogenetic protein 4 (hBMP4), 50 ng/ml human vascular endothelial growth factor-165 (hVEGF<sub>165</sub>), 20 ng/ml human stem cell factor (hSCF), and 10 μM Rock-inhibitor Y-27632 (Wako Chemicals, Neuss, Germany). The plate was centrifuged for 3 min at 100g. Half of the medium was changed on day 1 and day 2. Four days after initiation of EB formation, EBs with a diameter of ~500 μm were transferred to 6-well culture dishes coated with 0.1% gelatin (eight EBs per well) and containing 3 ml/well differentiation medium (X-VIVO 15 medium [Lonza, Verviers, Belgium], 2mM Ultraglutamine, 55 μM 2-mercaptoethanol, 1% Penicillin/Streptomycin [Pen/Strep], 25 ng/ml human interleukin 3 [hIL-3], 100 ng/ml human macrophage colony-stimulating factor [hM-CSF] [R&D Systems, Minneapolis, MN, USA]). Once per week, produced monocyte-like suspension cells were harvested and myeloid-cell-forming complexes (MCFCs) were supplied with 2 ml/well fresh medium. For terminal osteoclast differentiation, harvested monocyte-like cells were seeded at a density of  $1 \times 10^5$  cells/cm<sup>2</sup> in cell culture vessels supplied with α minimum essential medium (α-MEM) Eagle medium (Lonza, Verviers, Belgium) containing 10% fetal bovine serum (FBS) Superior (Sigma-Aldrich, St. Louis, MO, USA), 1% Pen/Strep, and 50 ng/ml hM-CSF. Three days after seeding, half of the culture medium was replaced with fresh osteoclast medium (α-MEM Eagle, 10% FBS Superior, 1% Pen/Strep, 100 ng/ml hM-CSF, 100 ng/ml human soluble receptor activator of nuclear factor-κ B ligand [hsRANKL]). Due to one half remaining old culture medium, the final cytokine concentration of freshly added hM-CSF and hsRANKL in the culture was 50 ng/ml. The cells were cultured for additional 3 to 7 days. Every 2 to 3 days, half of the medium was replaced with fresh osteoclast medium. All cytokines were purchased from Peprotech (Rocky Hill, NJ, USA) if not indicated differently. The procedure was adapted from a hiPSC-based macrophage differentiation protocol.<sup>(17)</sup>

### Isolation and differentiation of primary blood monocytes

PBMCs were isolated from whole blood of two healthy donors (female donor P1 and male donor P2) by density centrifugation (Biocoll, 1.077 g/ml; Merck Millipore, Molsheim, France), followed by MACS cell separation for monocyte enrichment (Monocyte Isolation Kit II; Miltenyi Biotec, Bergisch Gladbach, Germany). Freshly isolated primary monocytes underwent terminal osteoclast differentiation as described for hiPSCs in the previous paragraph.

### Flow cytometry

Surface marker staining of  $5 \times 10^5$  freshly isolated monocytes or harvested hiPSC-derived monocyte-like cells was performed in 50 μl staining solution for 10 min at 4°C. The staining solution contained Miltenyi Biotec (Bergisch Gladbach, Germany) antibodies and reagents diluted as indicated in fluorescence-activated cell sorting (FACS) buffer (2mM EDTA and 0.5% bovine serum albumin [BSA] in Dulbecco's phosphate-buffered saline [DPBS]): human Tandem Signal Enhancer 1:17, human Fc receptor [FcR]-Blocking Reagent 1:5, and Isotype controls 1:10 or human surface marker antibodies (CD34-fluorescein isothiocyanate [FITC] 1:10, CD45-VioBlue 1:20, CD66b-phycoerythrin [PE]-Vio770 1:20, CD11b-PE 1:50, CD14-allophycocyanin [APC] 1:50). Cells were washed with FACS buffer once before and three times after staining. Directly before sample acquisition by MACSQuant<sup>®</sup> VYB Analyzer (Miltenyi Biotec), cells were stained

with propidium iodide (1 μg/ml, Molecular Probes, Eugene, OR, USA) in 200 μl sample volume. Acquired data were analyzed with FlowJo 10.5.3 (FlowJo, LLC, Ashland, OR, USA). Debris, dead cells and cell doublets were excluded from the analysis as shown in the representative gating strategy in Figure S1.

### Osteoclast staining

Osteoclasts were fixed with 4% paraformaldehyde (PFA) 4 days after detection of the first osteoclasts in the culture. Staining of tartrate resistant acid phosphatase (TRAcP) activity was performed using Naphthol AS-MX phosphate disodium salt (Sigma-Aldrich, Taufkirchen, Germany) and Fast Red Violet LB Salt (Sigma-Aldrich, Taufkirchen, Germany). Actin was stained with fluorescently labeled phalloidin (Alexa Fluor<sup>™</sup> 488; Molecular Probes, Eugene, OR, USA) and 4',6-diamidino-2-phenylindole (DAPI; Life Technologies, Bleiswijk, Netherlands) detected the cell nuclei. Staining was performed as described.<sup>(18)</sup>

### Resorption assay

Two days after the first osteoclasts were detected in the culture, small mature osteoclasts were detached by Accutase treatment (Sigma-Aldrich, Taufkirchen, Germany) for 10 to 15 min at 37°C and seeded at a density of  $6.6 \times 10^4$  osteoclasts per 96-well either on dentine slices or cortical bovine bone slices (BoneSlices.com, Jelling, Denmark) in α-MEM Eagle medium containing 10% FBS Superior, 1% Pen/Strep, and 50 ng/ml hM-CSF and hsRANKL. Osteoclast cultures were maintained for 5 days. After 2 days, half of the medium was replaced with fresh one. At culture termination, bone slices were washed in purified water and cells were removed with a paper towel. Resorption pits were stained with either 0.25% toluidine solution (Sigma-Aldrich, Taufkirchen, Germany) or black ink (Pelikan, Feusisberg, Switzerland) for 15 s. The identification of pits, trenches, pseudoresorption, and the quantification was done as shown in Figure S2 and as described.<sup>(19)</sup> All quantification experiments were performed blinded.

### Quantitative reverse transcription polymerase chain reaction

RNA was extracted from the cells and purified by using the Direct-zol<sup>™</sup> RNA MiniPrep Kit (Zymo Research, Freiburg, Germany). Total complementary DNA (cDNA) was transcribed by RevertAid<sup>™</sup> H Minus First Strand cDNA Synthesis Kit (Life Technologies, Bleiswijk, Netherlands) using random hexamer primers. Quantitative polymerase chain reaction (qPCR) was performed with 5× HOT FIREPol<sup>®</sup> EvaGreen<sup>®</sup> qPCR Mix Plus (Solis BioDyne, Tartu, Estonia) on Quant Studio 3 Real-Time PCR System (Life Technologies, Singapore). Data were analyzed according to the delta-delta threshold cycle (ΔΔCt) method, whereby glyceraldehyde-3-phosphate dehydrogenase (*GAPDH*) levels served as internal controls. Primer sequences are listed in Table S2.

### Quantitative analysis of osteoclasts

Images of stained osteoclasts of three independent differentiation experiments of each cell line were taken using the Opera Phenix high content screener (Perkin Elmer, Waltham, MA, USA) and quantified. Three technical replicates of each differentiation and two pictures (one with high and one with low osteoclast density, each covering 6.5 mm<sup>2</sup>) of each replicate were

analyzed. By using image analysis software (CellProfiler; <https://cellprofiler.org/>) nuclei were identified, osteoclast cells were selected manually, and osteoclast number and size were quantified. On average, 812 osteoclasts per cell line and experiment were analyzed. All quantification experiments were performed blinded.

### Lysosomal pH measurement

Lysosomal pH was measured essentially as described.<sup>(7)</sup> Human iPSCs were dissociated to single cells using TrypLE Select Enzyme and seeded onto glass-bottom live-cell dishes (MatTek, Ashland, MA, USA) in Essential 8 medium supplemented with 10 $\mu$ M Rock-inhibitor Y-27632. Twenty-four hours (24 h) after plating, lysosomes were loaded with 0.5 mg/ml Oregon Green 488-dextran (Life Technologies, Bleiswijk, Netherlands) in growth medium overnight, followed by a 2 h chase. For imaging, the medium was changed to imaging buffer containing 135mM NaCl, 5mM KCl, 1mM MgCl<sub>2</sub>, 1mM CaCl<sub>2</sub>, and 10mM glucose, 10mM *N*-2-hydroxyethylpiperazine-*N'*-2-ethanesulfonic acid (HEPES), pH 7.4. Images were acquired using a Leica DMI8 microscope (Leica Microsystems, Wetzlar, Germany) equipped with a 63  $\times$  1.40 numerical aperture (NA) oil-immersion lens and an Oregon Green filter cube (AHF analysentechnik AG, Tübingen-Pfrondorf, Germany) with excitation at 440 or 480 nm, respectively, delivered by an OptoScan monochromator (Cairn Research, Faversham, UK) controlled by the microscopy software WinFluor (John Dempster, University of Strathclyde, Glasgow, Scotland), and emission at 516 to 556 nm. At the end of each experiment, in situ pH calibration curves were obtained in isotonic K-based solutions (5mM NaCl, 115mM KCl, 1.2mM MgSO<sub>4</sub>, 10mM glucose, 25mM of either HEPES, 2-(*N*-morpholino)ethanesulfonic acid [MES], or acetate, ranging in pH from 3.9 through 6.5) supplemented with 10 $\mu$ M of both nigericin and monensin after equilibration for at least 2 min for each pH. Images were analyzed using ImageJ software (NIH, Bethesda, MD, USA; <https://imagej.nih.gov/ij/>), where regions of interest (ROIs) were defined as areas above a defined fluorescence threshold in the acquired images at 440 nm excitation (pH-insensitive). The mean intensity ratio between 480 and 440 nm excitation was calculated after background subtraction for each ROI. The fluorescence intensity ratios (488/440) as a function of pH was fit to a sigmoid and used to interpolate the pH values from the cells prior to the calibration.

### Immunostaining

Plasmid DNA encoding the respective constructs (hCIC-7 wild-type [WT] or mutant, and human OSTM1 (hOSTM1)–monomeric red fluorescent protein (mRFP) was transfected into HeLa cells at 40% confluency, using Fugene 6 reagent (Promega, Madison, WI, USA), 48 h before fixation with 4% PFA in PBS for 15 min. For immunolabeling, cells were incubated with 30mM glycine in PBS for 5 min, permeabilized with antibody buffer (0.05% saponin and 3% BSA in PBS) for 15 min and then subsequently incubated with primary and AlexaFluor-coupled secondary antibodies diluted in antibody buffer for 90 and 60 min, respectively, with washing steps in antibody buffer. Primary antibodies were rabbit anti-CIC-7 (7N4B; kind gift from Thomas Jentsch<sup>(5)</sup>) and mouse anti-lysosomal-associated membrane protein 1 (anti-LAMP-1) (H4A3 was deposited to the DSHB by August, J.T. / Hildreth, J.E.K. [DSHB Hybridoma Product H4A3]). Images were acquired with a Leica DMI8 light microscope (Leica

Microsystems, Wetzlar, Germany) equipped with a 63  $\times$  1.40 NA oil-immersion lens and respective filter cubes (FITC for Alexa488; tetramethylrhodamine isothiocyanate [TRITC] for mRFP; and Y5.5 [filter cube] for Alexa633).

### Electrophysiology

hCIC-7 and h-OSTM1-mRFP expressing plasmids were co-transfected in HEK-293 cells by using Effectene Transfection Reagent (Qiagen, Hilden, Germany). Patch-clamp experiments were performed in whole-cell configuration 24 to 72 h posttransfection. Pipettes were pulled from borosilicate capillaries (Hilgenberg, Malsfeld, Germany) and had a resistance of 1.5 to 2.5 MOhm in measuring solutions. The standard intracellular (pipette) solution contained (in mM) 130 NaCl, 10 HEPES, 2 MgSO<sub>4</sub>, and 2 EGTA (pH 7.3). The extracellular (bath) solution contained (in mM) 147 NaCl, 10 HEPES, and 4 MgSO<sub>4</sub> (pH 7.3). Voltage steps of 1 s duration from 120 to 60 mV in decrements of 20 mV with 1 s interval between pulses were conducted, holding potential was 0 mV. Data were acquired at 20 to 50 kHz after filtering at 10 kHz with an eight-pole Bessel filter using an Axopatch 200 amplifier (Molecular Devices, San Jose, CA, USA) with GePulse software. Data analysis was performed with Ana software (GePulse and Ana available at: <http://users.ge.ibf.cnr.it/pusch/>).

### Plasmids

The expression plasmid for hCIC-7 was described.<sup>(20)</sup> The mutations p.(G292E) and p.(R403Q) were introduced by recombinant PCR. For patch-clamp experiments, four additional mutations deleting lysosomal targeting di-leucine motifs (leucine 23, 24, 68, and 69 changed to alanines) were introduced into *CLCN7*.<sup>(21)</sup> For expression of hOSTM1-mRFP, the open reading frame (ORF) was cloned into pmRFP-N1. The complete ORFs were confirmed by Sanger sequencing.

### LC3 and CIC-7 Western blot

For the analysis of the autophagic markers like microtubule-associated protein light chain 3 (LC3)-I and II and the determination of the autophagic flux, hiPSCs were seeded at about 70% confluency. The next day, cells were starved for 2 h in Krebs-Ringer solution (Alfa Aesar; Thermo Fisher, Kandel, Germany) and incubated with or without 50 $\mu$ M chloroquine (autophagy inhibitor). Cells were lysed with radioimmunoprecipitation assay (RIPA) buffer containing cOMplete™ protease inhibitors (Roche, Mannheim, Germany) and the proteins LC3 (Cell Signaling Technology, Beverly, MA, USA; #4108, 1:1000) and GAPDH (Thermo Fisher Scientific; #AM4300, 1:20,000) were analyzed by immunoblotting after 12% sodium dodecyl sulfate–polyacrylamide gel electrophoresis (SDS-PAGE) and transferred to a polyvinylidene fluoride (PVDF) membrane. GAPDH and LC3-II levels were determined by densitometric quantification and LC3-II was normalized to GAPDH. For each culture condition (standard and starvation), the autophagic flux was calculated by subtracting densitometrically quantified relative LC3-II levels obtained without chloroquine treatment from LC3-II levels acquired with chloroquine.<sup>(22)</sup> For CIC-7 immunoblotting hiPSCs were lysed, separated, blotted, and quantified as described earlier in this paragraph for LC3 Western blot analysis. A total of 20  $\mu$ g of protein per lane was separated by 10% SDS-PAGE and blotted proteins were probed with following antibodies: guinea-pig anti CIC-7



(7N4B<sup>5</sup>); gift from Thomas Jentsch) and rabbit anti GAPDH (14C10; Cell Signaling Technology; #2118, 1:1,000).

### Statistical analysis

Data were plotted and statistically evaluated using GraphPad Prism Version 8 (GraphPad Software, Inc., La Jolla, CA, USA).

## RESULTS

### Efficient generation of monocyte-like cells from hiPSC-derived myeloid-cell-forming complexes

To establish an efficient osteoclast differentiation protocol, we used two hiPSC lines (BIHi001-A and BIHi004-A), derived from skin fibroblasts of healthy control individuals. The first differentiation step was induced via the formation of embryoid bodies (EBs) in ultra-low attachment plates (Figure 1A). Next, a

combination of hBMP4, hVEGF, and hSCF initiated mesodermal priming of EBs. In order to monitor the differentiation process, we analyzed marker gene expression by quantitative reverse transcription polymerase chain reaction (qRT-PCR). Comparing undifferentiated hiPSCs and EBs, we observed successful mesodermal induction by decreased expression of pluripotency markers *OCT4*, *SOX2*, and *NANOG*, and increased expression of mesodermal markers *CD34*, *HAND1*, *TBXT*, and *CDX2* (Figure 1B, Figure S3).

As a second step, EBs were differentiated into myeloid-cell-forming complexes (MCFCs). Depending on the hiPSC line, over a time period of 9 to 13 weeks, MCFCs were exposed to hIL-3 and hM-CSF, which triggered the release of suspension cells into the medium (Figure 1A). Between weeks 2 and 3, our tested hiPSC lines showed the highest suspension cell release (up to  $7.5 \times 10^5$  cells per well containing eight MCFCs). After this production peak, the number of suspension cells slowly decreased (Figure 2A). On average, every MCFC released  $3.2 \times 10^5$

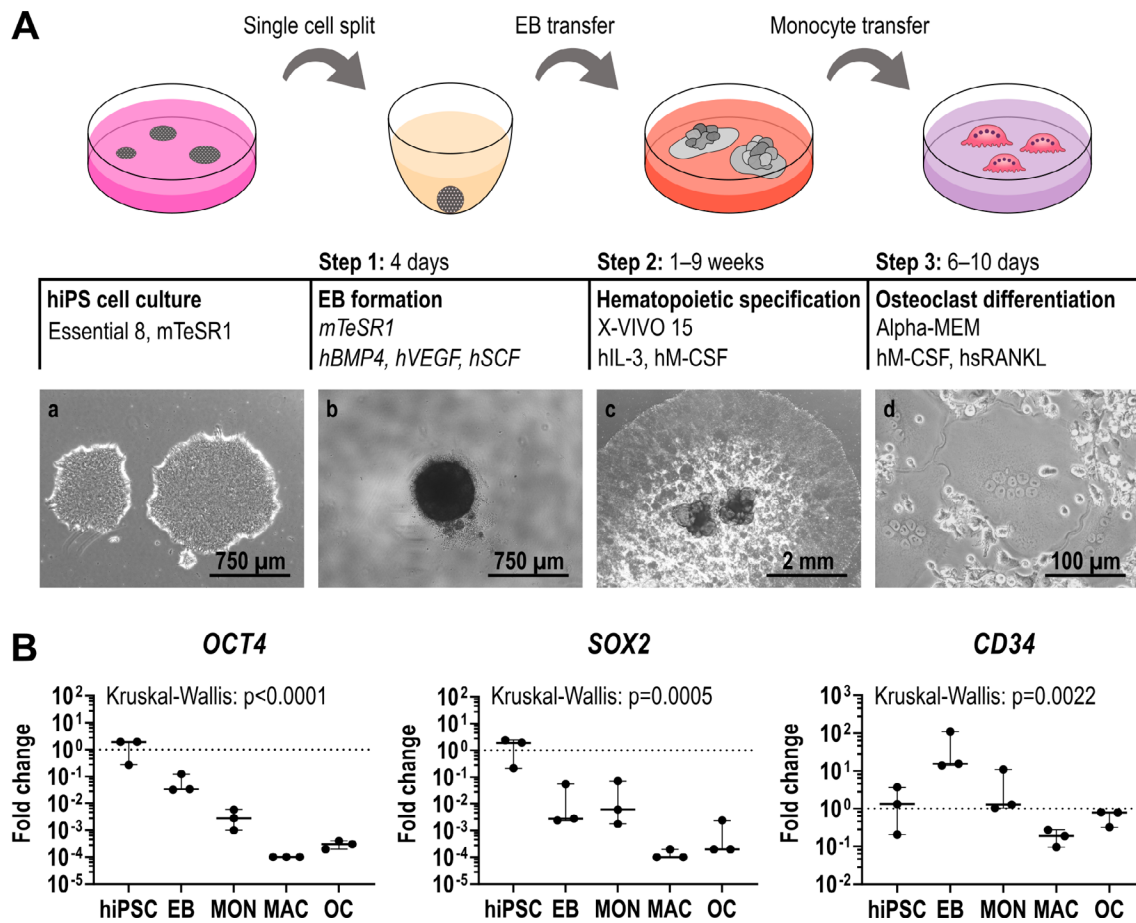


**FIGURE 1.** Differentiation of hiPSCs into osteoclasts. (A) Schematic illustration of the osteoclast differentiation procedure. Step 1: EB formation. Step 2: Differentiation of EBs into MCFCs, which produce monocyte-like suspension cells. Step 3: Final osteoclast differentiation of monocyte-like cells. Phase contrast images of hiPSC colonies (a), a single EB (b), MCFCs (c), and osteoclasts (d). (B) Expression of pluripotency markers *OCT4* and *SOX2* and mesodermal marker *CD34* determined by qRT-PCR analysis in BIHi004-A hiPSC-derived cells in undifferentiated hiPSCs, 4-day-old EBs, MONs, MACs, and OCs. Expression is normalized to hiPSCs, *GAPDH* expression was used as housekeeping control. Data show box-plots with median, interquartile range, maximum, and minimum values, and all data points of three independent experiments. For statistical analysis, Kruskal-Wallis test and Dunn's multiple comparisons were used (Table S3). Abbreviations: EB, embryoid body; *GAPDH*, glyceraldehyde-3-phosphate dehydrogenase; hiPSC, human induced pluripotent stem cell; MAC, macrophage, MCFC, myeloid-cell-forming complex; MON, monocyte-like cell; OC, osteoclast; qRT-PCR, quantitative reverse transcription polymerase chain reaction.

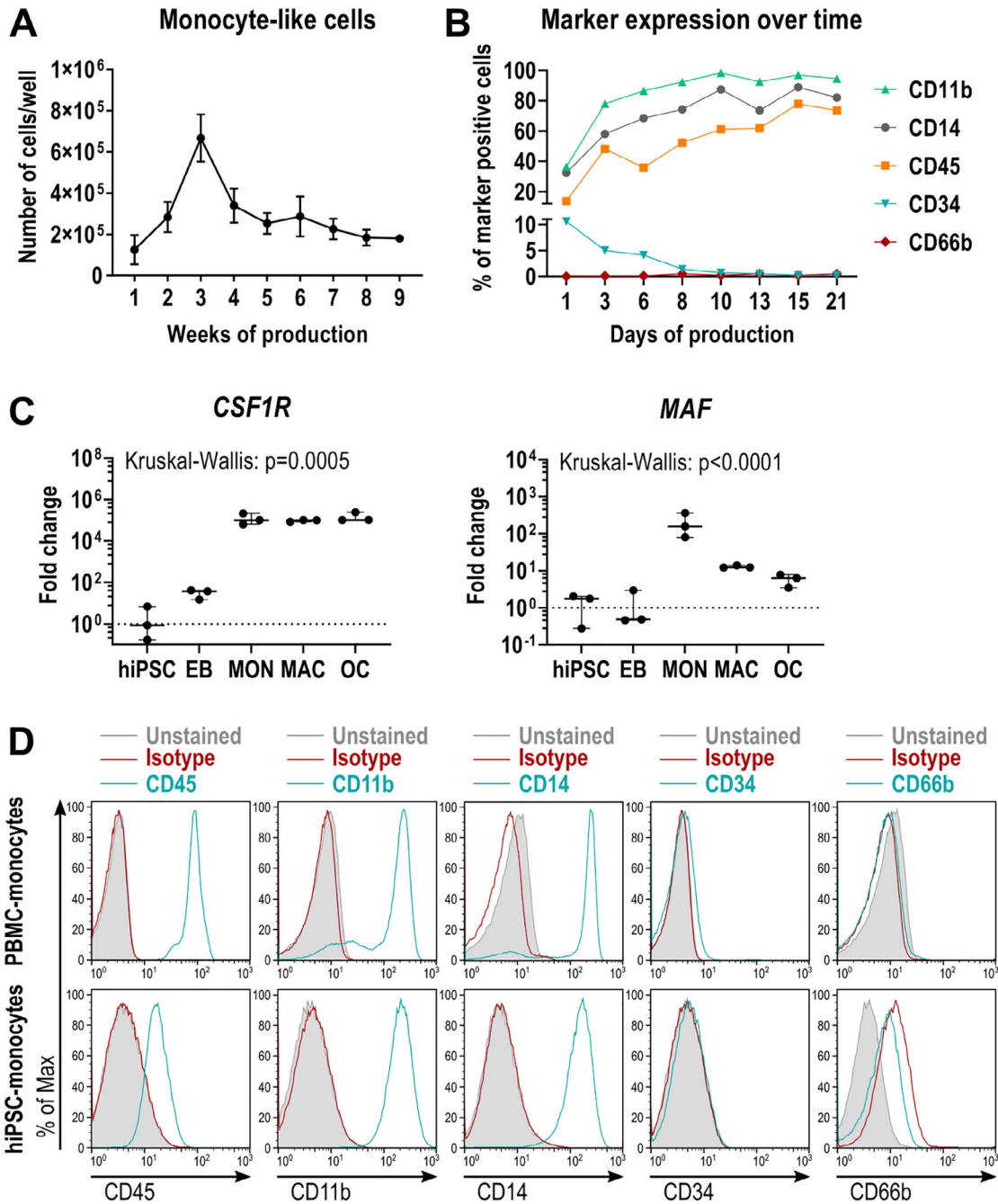


**FIGURE 2.** Characterization of hiPSC-derived monocyte-like cells. (A) Kinetics of monocyte-like cell production in BIHi004-A hiPSCs. Data are absolute numbers of harvested suspension cells per 6-well containing eight MCFCs (means and SD of three independent experiments, each with twelve 6-wells). (B) Frequency of surface marker-expressing monocyte-like cells determined by flow cytometry, harvested at different time points. (C) Expression of monocyte markers *CSF1R* and *MAF* determined by qRT-PCR analysis in BIHi004-A hiPSC-derived cells in undifferentiated hiPSCs, 4-day-old EBs, MONs, MACs, and OCs. Expression is normalized to hiPSCs, *GAPDH* expression was used as housekeeping control. Data show box-plots with median, interquartile range, maximum, and minimum values and all data points of three independent experiments. For statistical analysis, Kruskal-Wallis test and Dunn's multiple comparisons were used (Table S3). (D) Representative flow cytometry analysis of human primary monocytes (donor P2) and hiPSC-derived monocyte-like cells (BIHi004-A, harvested in week 5 after EB transfer). Histograms show unstained cells (gray-filled), cells stained with isotype controls (red), and cells stained with the respective surface markers (blue). Abbreviations: EB, embryoid body; *GAPDH*, glyceraldehyde-3-phosphate dehydrogenase; hiPSC, human induced pluripotent stem cell; MAC, macrophage, MCFC, myeloid-cell-forming complex; MON, monocyte-like cell; OC, osteoclast; qRT-PCR, quantitative reverse transcription polymerase chain reaction; SD, standard deviation.

suspension cells within 9 weeks. During the first days of production, flow cytometry showed a considerable fraction of CD34<sup>+</sup> cells, indicating an immature phenotype (Figure 2B, Figure S4). We also detected many dead cells during this early phase of the differentiation protocol (Table S4). The released cells gradually matured over the next 2 weeks. Around the time of maximal production, the suspension cells were positive for monocyte markers like CD11b, CD14, CD45, but negative for CD34 (marker for hematopoietic stem cells [HSCs]) and CD66b (marker for eosinophils and neutrophils). qRT-PCR also revealed an increased expression of the hM-CSF receptor *CSF1R* and *MAF* (involved in macrophage proliferation) when compared to undifferentiated hiPSCs and EBs (Figure 2C). Hence, the released cells closely resembled monocyte-like cells. Indeed, primary monocytes freshly isolated from peripheral blood displayed the same surface marker profile as hiPSC-derived monocyte-like cells (Figure 2D). In the final step of the protocol, the harvested monocyte-like cells were differentiated into osteoclasts by exposing them to hM-CSF and hRANKL (Figure 1A).

### Physiological gene expression and an increased size of hiPSC-derived osteoclasts

Next, we analyzed the hiPSC-derived osteoclasts for typical osteoclast features and functionality and compared them to osteoclasts differentiated from monocytes from PBMCs of healthy donors. First, TRAcP-Phalloidin-DAPI staining of PBMC-derived and hiPSC-derived osteoclasts differentiated by our protocol, revealed multinucleated TRAcP-positive cells and the formation of a podosome belt (Figure 3A, middle). Furthermore, both osteoclast types were able to form resorption pits and trenches on dentine (Figure 3A, right). Finally, osteoclast markers like cathepsin K (*CTSK*) and matrix metalloproteinase 9 (*MMP9*) were similarly upregulated in primary and hiPSC-osteoclasts, as demonstrated by transcriptome and qRT-PCR analysis (Figure S6, Figure 3B, Figure S5, Table S3, Table S5). A comparison of global expression signatures revealed close similarity between PBMC-derived and hiPSC-derived osteoclasts in comparison to monocytes (Figure S6). Among the genes with elevated expression in hiPSC-derived osteoclasts were *FOS*, *MAF*, and *NFATC1*. *MAF* is a macrophage marker gene and *FOS* is important for early differentiation of macrophages and osteoclasts.<sup>(23)</sup> We thus conclude that our differentiation protocol generated slightly immature osteoclasts that are fully functional.

To evaluate the efficiency of our osteoclast differentiation protocol and to investigate osteoclast morphology, we quantified the osteoclast yield in more detail. Interestingly, the time between seeding of monocytes and the formation of the first visible osteoclasts was highly dependent on the donor, but not on the origin (primary or hiPSC) of the cells (Figure S7, Table S7). Thus, in order to compare osteoclast differentiation and morphology between different donors, cells for quantitative analysis from all donors were fixed 4 days after the appearance of the first osteoclasts. Osteoclasts differentiated from hiPSCs covered a larger area of the culture dish surface than PBMC-derived osteoclasts (Figure 3C). In contrast, we determined that numbers of hiPSC-derived osteoclasts per area were lower compared to PBMC-derived osteoclasts (Figure 3D, right). The slightly bigger area covered by hiPSC-derived osteoclasts and the reduced number of osteoclasts/mm<sup>2</sup> was in line with an increased size of the osteoclasts and higher number of nuclei per osteoclast, when compared to PBMC-derived osteoclasts (Figure 3D,

Figure S8). Hence, hiPSC-derived osteoclasts seem to grow bigger in a shorter time period. Nevertheless, we observed no major difference in cell morphology between hiPSC-derived osteoclasts and osteoclasts differentiated from PBMCs. We estimate that, using our differentiation protocol, we are able to generate 4640 osteoclasts (nine nuclei on average) out of one hiPSC within 3 months.

### Subtle differences in resorption behavior of hiPSC-derived osteoclasts

For further characterization of the resorption ability of hiPSC-derived osteoclasts, we cultured osteoclasts this time on cortical bone slices instead of dentine, because bovine bone is a more physiological substrate. We showed that there are no significant differences in the total amount of eroded bone surface (Figure 3E left, Table S8). However, there was an insignificant trend toward more bone resorption made by hiPSC-derived osteoclasts (around 5% of the bone surface) compared to PBMC-derived osteoclasts (around 3% of the bone surface). Interestingly, we detected that hiPSC-osteoclasts only superficially eroded 2% of the bone surface (pseudoresorption; Figure S2), whereas for primary osteoclasts this was at a comparable level around 1% (Figure 3E, right). Furthermore, we found that the morphology of the resorption cavities formed by hiPSC-osteoclasts from different healthy donors were variable: although BIHi004-A formed around 60% trenches and 40% pits, BIHi001-A only generated 20% trenches and 80% pits (Figure 3E, middle). The resorption pattern of primary osteoclasts showed an even lower proportion of trenches (10%) and up to 90% pits.

To test our established protocol with additional hiPSC lines, we generated the hiPSC lines isWT1 and isWT7 from dermal fibroblasts of healthy donors. The detailed characterization of the isWT1 and isWT7 hiPSCs proved their pluripotency (Figure S9), differentiation potential (Figure S10), and chromosomal stability (Figure S11 and S12). Applying our differentiation protocol to isWT1 and isWT7 cells and one additional hiPSC line led to terminally differentiated and bone-resorbing osteoclasts (Figure S13), demonstrating the robustness of our method.

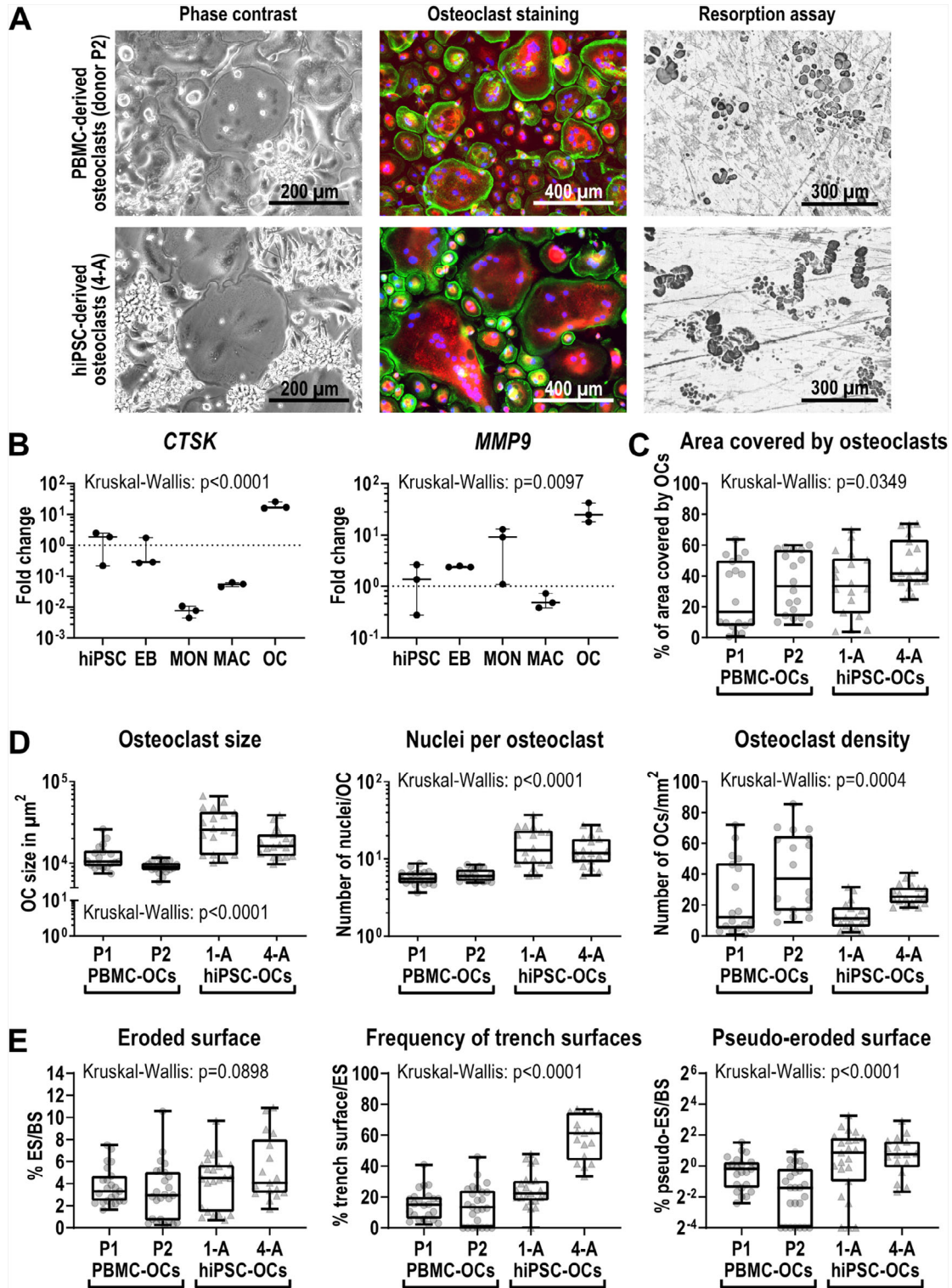
### A case of lethal neuronopathic ARO with brain malformation due to compound heterozygous missense mutations in the *CLCN7* gene

The male infant was the second child of healthy nonconsanguineous white parents. Beyond the neonatal period from the age of 8 to 10 weeks he exhibited failure to thrive, reduced weight gain, muscular hypotonia, and nystagmus. At the age of 4 months, he developed refractory infantile spasms and progressive developmental delay. Electroencephalogram (EEG) revealed hypsarrhythmia and amplitude depression. The cranial magnetic resonance imaging (MRI) showed a mild reduction of brain volume and subependymal heterotopic bands indicating a neuronal migration disorder (Figure 4A,B). At the age of 7 months, the cerebral ultrasound revealed progressive brain atrophy and a hydrocephalus ex vacuo. Retinal pigmentary changes were diagnosed in funduscopy. A chest x-ray showing generalized bone sclerosis hinted toward a neuronopathic form of osteopetrosis (Figure 4C). In the further course of the disease, the infant developed a spastic tetraparesis, dysphagia, and chronic respiratory failure. From the age of 8 months, he had a mild hypochromic anemia. Candidate gene analysis by Sanger sequencing



detected the mutations c.875G>A, p.(G292E) and c.1208G>A, p.(R403Q) in the *CLCN7* gene in a compound heterozygous state (Figure 4D). Although the latter mutation has already been described in an ARO patient,<sup>(24)</sup> the c.875G>A mutation was novel. The affected glycine residue is evolutionarily conserved

and flanking missense mutations have been previously identified in ARO patients.<sup>(25)</sup> The child deceased at the age of 14 months as a consequence of progressive respiratory failure. Given the exceptional phenotype of ARO, with predominant neurological symptoms and impaired cortical development, we





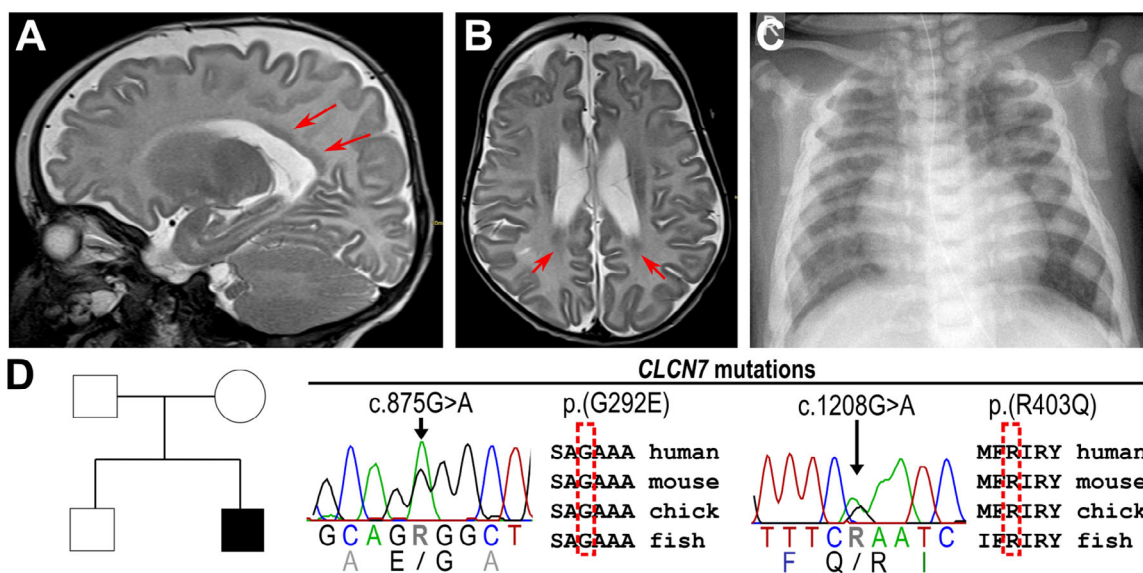


**FIGURE 4.** Radiologic images of an ARO patient with compound heterozygous mutations in the *CLCN7* gene. (A) T2W sagittal MRI and (B) axial MRI of the head of 4-month-old patient with reduced brain volume and periventricular laminar subependymal heterotopias (red arrows). (C) Chest x-ray of 7-month-old patient showing sclerosis and plump configuration of the ribs. (D) Pedigree of the affected family carrying the heterozygous missense mutations c.875G>A p.(G292E) and c.1208G>A p.(R403Q) in conserved regions of the *CLCN7* gene. Abbreviations: ARO, autosomal recessive osteopetrosis; MRI, magnetic resonance imaging; T2W, T2-weighted.

decided to generate ARO hiPSCs from blood cells for follow-up investigations (cell line BIHi002-A<sup>(16)</sup>).

#### Reduced stability and residual lysosomal localization of the mutated CIC-7 protein showing reduced ion currents

The pronounced neurological phenotype was reminiscent of patients with an activating CIC-7 mutation, impairing lysosomal function and reportedly enhancing lysosomal acidification.<sup>(9)</sup> To decipher the functional consequences of the identified mutations, we first overexpressed both p.(G292E) and p.(R403Q) CIC-7 in HeLa cells. This approach revealed normal lysosomal localization and co-localization with OSTM1 of the mutated proteins (Figure 5A, Figure S14). We next analyzed *CLCN7* expression levels in undifferentiated ARO hiPSCs in comparison to control

hiPSCs. We could not detect any differences in *CLCN7* expression at the RNA level (Figure S15, Table S9), whereas immunoblot analysis showed a reduction of CIC-7 protein levels by 70% in ARO hiPSCs (Figure 5B, Figure S16). However, because residual expression and physiological localization of the CIC-7 protein were still detectable, we wondered about the electrophysiological features of the mutated Cl<sup>-</sup>/H<sup>+</sup>-exchanger. In comparison to WT CIC-7 protein, overexpression of the mutants in HEK-293 cells revealed an ion current density reduced to 13% in cells expressing the CIC-7 p.(R403Q) protein, whereas ion conductance was completely abolished in CIC-7 p.(G292E)-expressing cells (Figure 5C, Figure S17). In aggregation, the mutations lead to lower CIC-7 protein levels and strongly reduced ion currents hinting primarily at a loss-of-function pathomechanism.

**FIGURE 3.** Characterization of differentiated hiPSC-derived osteoclasts. Osteoclasts were differentiated from PBMCs (donors P1 and P2) and the two hiPSC lines BIHi001-A (1-A) and BIHi004-A (4-A). (A) Representative images of osteoclasts in culture (phase contrast), stained osteoclasts (Phalloidin in green, TRAcP in red, DAPI in blue) and osteoclast-mediated resorption shown as black-stained cavities on dentine. (B) Expression of osteoclast markers *CTSK* and *MMP9* determined by qRT-PCR analysis in BIHi004-A hiPSC-derived cells in undifferentiated hiPSCs, 4-day-old EBs, MONs, MACs, and OCs. Expression is normalized to hiPSCs, *GAPDH* expression was used as housekeeping control. Shown are data of three independent experiments. For statistical analysis, Kruskal-Wallis test and Dunn's multiple comparisons were used (Table S3). (C,D) Quantitative analysis of osteoclast morphology parameters. Shown are pooled data from three independent experiments. For statistical analysis, Kruskal-Wallis test and Dunn's multiple comparisons were used (Table S6). (C) Percentage of area covered by osteoclasts of total well area. (D) Osteoclast size in  $\mu\text{m}^2$  (left), number of nuclei per osteoclast (middle) and osteoclast density (right). (E) Analysis of the resorption pattern on cortical bone slices. Percentage of the ES to the BS (left), percentage of the trench surface to the total eroded surface (middle), and percentage of the pseudo-eroded surface to the total bone surface (right). Shown are pooled data of individual bone slices used in three independent differentiation experiments of each cell line (donor P1 and 1-A  $n = 23$ , donor P2  $n = 25$ , 4-A  $n = 17$ ). Significance was calculated using Kruskal-Wallis and Dunn's multiple comparisons test (Table S8). Box-plots shown in B–E are plotted with median, interquartile range, maximum, and minimum values and all data points. Abbreviations: BS, total bone surface; DAPI, 4',6-diamidino-2-phenylindole; EB, embryoid body; ES, eroded bone surface; *GAPDH*, glyceraldehyde-3-phosphate dehydrogenase; hiPSC, human induced pluripotent stem cell; MAC, macrophage, MCFC, myeloid-cell-forming complex; MON, monocyte-like cell; OC, osteoclast; PBMC, peripheral blood mononuclear cell; qRT-PCR, quantitative reverse transcription polymerase chain reaction; TRAcP, tartrate resistant acid phosphatase.

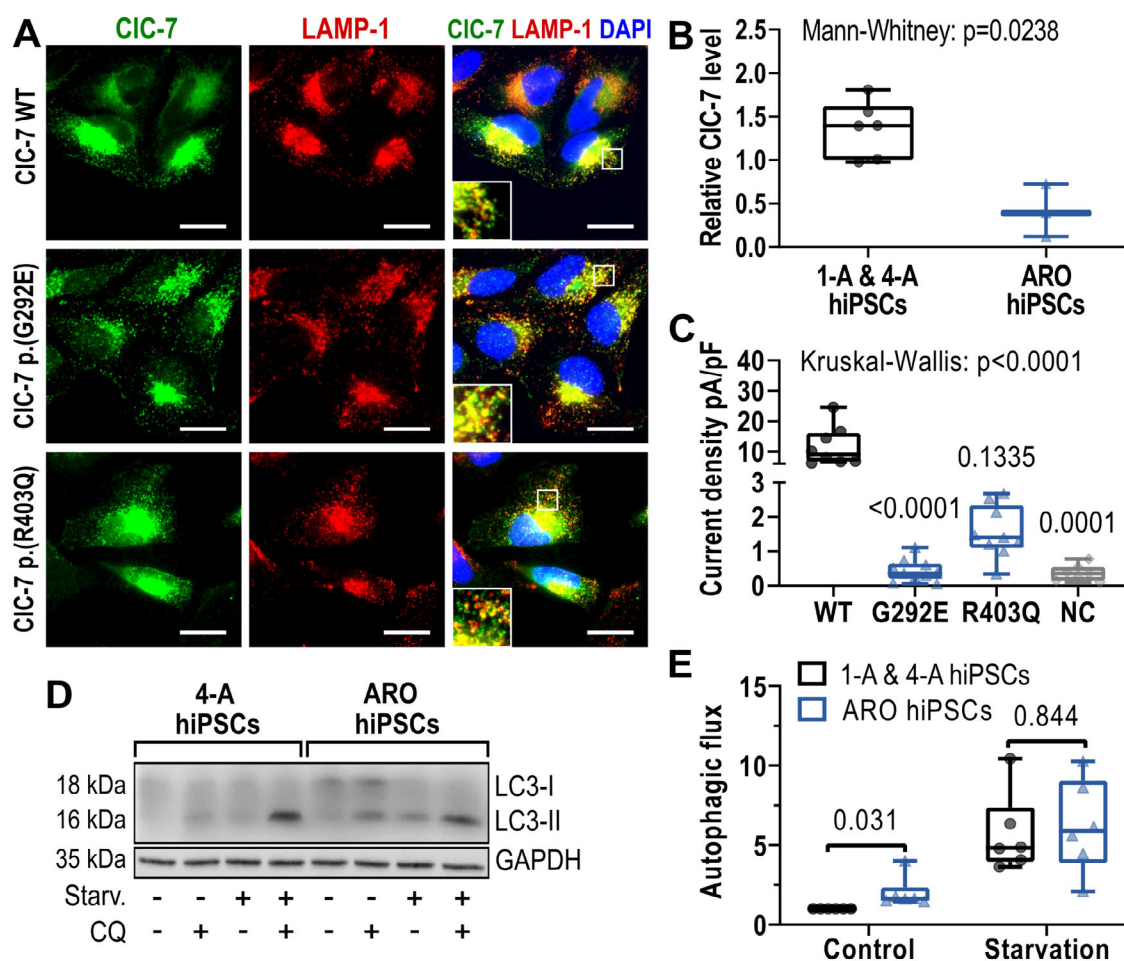


**FIGURE 5.** Characterization of the degradative pathway in *CLCN7* mutant cells. (A) Subcellular localization of CIC-7 in HeLa cells transfected with WT or mutated hCIC-7 shown by immunostaining: Anti-CIC-7 (green), late endosomal/lysosomal marker anti-LAMP-1 (red), DAPI (blue). Scale bar = 25  $\mu\text{m}$ . (B) Densitometric quantification of relative CIC-7 protein levels in undifferentiated control hiPSCs BIHi001-A (1-A) and BIHi004-A (4-A) and ARO (representative immunoblot shown in Figure S16). Shown are data of three independent experiments (pooled data points of control hiPSCs). CIC-7 levels were quantified against the loading control GAPDH. Significance was calculated by Mann-Whitney test (control hiPSCs 1-A and 4-A  $n = 6$ , ARO hiPSCs  $n = 3$ ). (C) Electrophysiological analysis in HEK-293 cells co-transfected with OSTM1 and either WT or mutated (G292E or R403Q) hCIC-7. Untransfected cells served as NC. Values of  $p$  shown were calculated with Dunn's multiple comparisons (compared to WT). (D) Representative LC3 immunoblot of BIHi004-A and ARO hiPSCs under control culture conditions or starvation with or without autophagy inhibitor CQ. (E) Autophagic flux in BIHi001-A, BIHi004-A, and ARO hiPSCs under normal culture conditions and starvation determined by relative LC3-II protein levels. Shown are pooled data of three independent experiments ( $n = 6$ ), which were normalized to BIHi001-A and BIHi004-A in control culture conditions. Significance was calculated by Wilcoxon matched-pairs signed rank test. Box-plots shown in B, C, and E are plotted with median, interquartile range, maximum, and minimum values and all data points. Abbreviations: ARO, autosomal recessive osteopetrosis; CQ, chloroquine; DAPI, 4',6-diamidino-2-phenylindole; GAPDH, glyceraldehyde-3-phosphate dehydrogenase; hiPSC, human induced pluripotent stem cell; LAMP-1, lysosomal-associated membrane protein 1; LC3, microtubule-associated protein light chain 3; NC, negative control; OSTM1, osteopetrosis-associated transmembrane protein 1; WT, wild-type.

Lysosomes play a fundamental role in autophagy by fusing with autophagosomes to form autolysosomes. Our analysis of the lysosomal pH in ARO hiPSCs revealed no significant differences compared to control hiPSCs (Figure S18). Nevertheless, we detected an increased level of the autophagy marker LC3-II in undifferentiated ARO hiPSCs under standard culture conditions (Figure 5D, Figure S18, Figure S19). To determine the autophagic flux, we both induced autophagy by starvation and inhibited the further processing of LC3-II by chloroquine treatment.<sup>(22)</sup> Although ARO hiPSCs displayed a higher autophagic flux at control conditions, there was no difference to control

hiPSCs under starvation (Figure 5E). Because elevated LC3-II levels have been described also for murine *Cln7*-deficient tissues,<sup>(6)</sup> this further corroborates a loss-of-function effect.

#### ARO hiPSCs form enlarged osteoclasts with normal marker gene expression, but without resorptive activity

As a test case for our in vitro model system, we applied the established osteoclast differentiation protocol to the patient-derived ARO hiPSCs. During all steps of differentiation ARO hiPSCs showed expression of the typical markers like hiPSCs of healthy

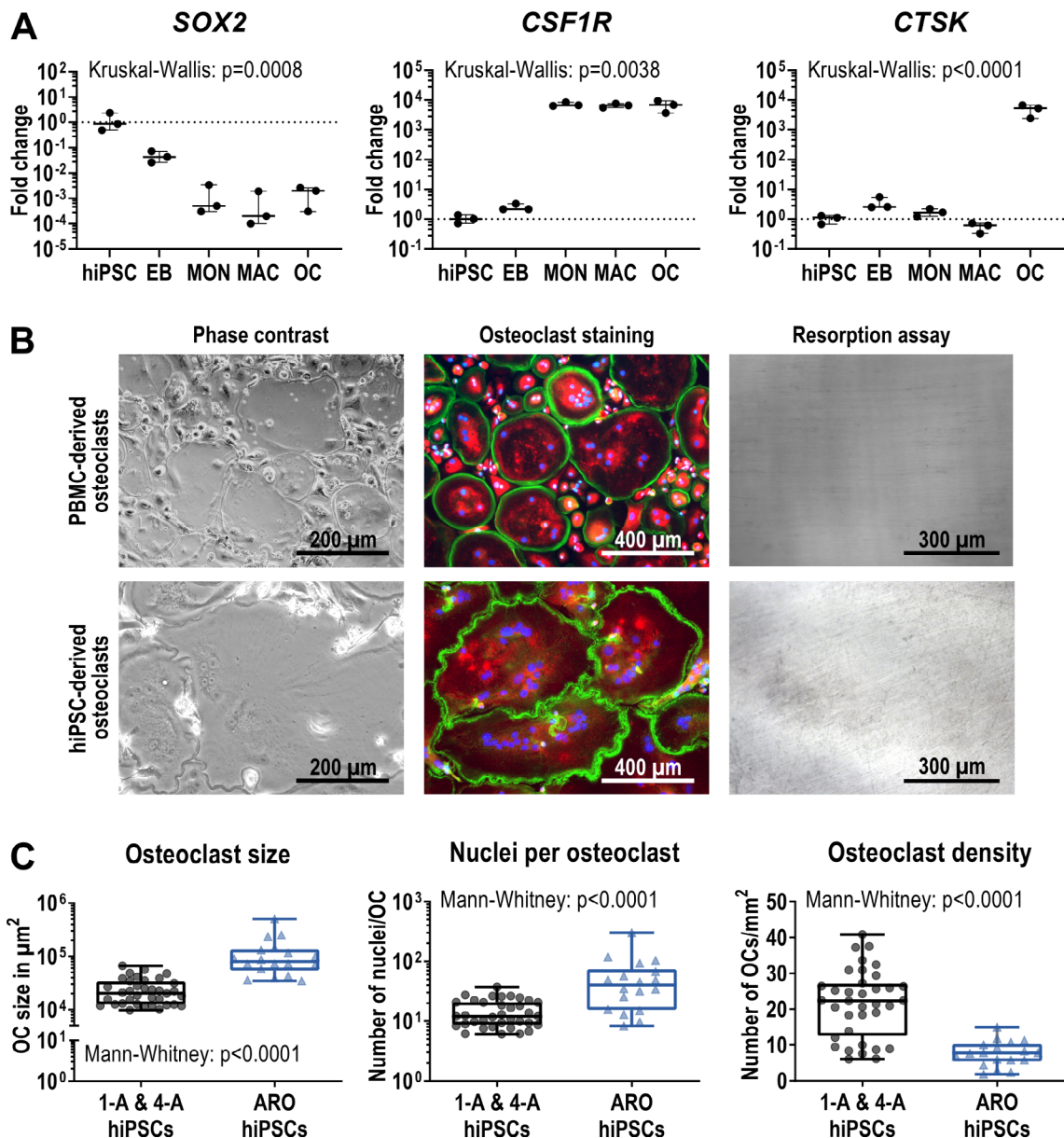


**FIGURE 6.** Characterization of osteoclasts differentiated from ARO hiPSCs. (A) Expression of pluripotency marker *SOX2*, monocytic marker *CSF1R* and osteoclast marker *CTSK* determined by qRT-PCR analysis in ARO hiPSC-derived cells in undifferentiated hiPSCs, 4-day-old EBs, MONs, MACs, and OCs. Expression is normalized to hiPSCs, *GAPDH* expression was used as housekeeping control. Shown are data of three independent experiments. For statistical analysis, Kruskal-Wallis test and Dunn's multiple comparisons were used (Table S10). (B) Representative images showing osteoclasts in culture (phase contrast), stained osteoclasts (Phalloidin in green, TRAcP in red, DAPI in blue) and lack of osteoclast-mediated resorption (resorption assay shows no black stained resorption cavities on dentine, see Figure 3A for comparison). Osteoclasts were differentiated from ARO patient-derived PBMCs and BIHi002-A ARO hiPSCs. (C) Osteoclasts differentiated from BIHi001-A (1-A), BIHi004-A (4-A), and ARO hiPSCs quantified according to their size in  $\mu\text{m}^2$  (left), the number of nuclei per osteoclast (middle), and the osteoclast density (right). Shown are pooled data of three independent differentiation experiments of each cell line (control hiPSCs 1-A and 4-A  $n = 36$ , ARO hiPSCs  $n = 18$ ). Significance was calculated using Mann-Whitney test. Box-plots shown in A and C are plotted with median, interquartile range, maximum, and minimum values and all data points. Abbreviations: ARO, autosomal recessive osteopetrosis; DAPI, 4',6-diamidino-2-phenylindole; EB, embryoid body; hiPSC, human induced pluripotent stem cell; MAC, macrophage; MON, monocyte-like cell; PBMC, peripheral blood mononuclear cell; OC, osteoclast; qRT-PCR, quantitative reverse transcription polymerase chain reaction; TRAcP, tartrate resistant acid phosphatase.

controls (Figure 6A, Figure S20A). The production of  $\text{CD45}^+$ ,  $\text{CD11b}^+$ ,  $\text{CD14}^+$  monocyte-like cells was even better than in BIHi004-A hiPSCs and peaked at  $1 \times 10^6$  cells/well in week three

(Figure 2A, Figure S20B,C). ARO osteoclasts were large, multinucleated TRAcP-positive cells forming a podosome belt and exhibited high expression of *CTSK* and *MMP9* (Figure 6A,B,



Figures S20A and S21). In addition, we also differentiated osteoclasts from PBMCs derived from the same patient. No significant differences in morphology or characteristics in the TRAcP-Phalloidin-DAPI staining were detectable between both osteoclasts (Figure 6B). Our quantification analysis revealed that osteoclasts differentiated from ARO hiPSCs had a larger diameter and displayed higher numbers of nuclei compared to hiPSC-osteoclasts from healthy controls (BIHi001-A and BIHi004-A), resulting in a lower number of osteoclasts per surface unit (Figure 6C). Notably, compared to the healthy control (Figure 3A), neither PBMC-derived nor hiPSC-derived ARO osteoclasts showed any sign of bone resorption activity (Figure 6B), suggesting that ARO hiPSC-derived osteoclasts reproduced the expected cellular phenotype.

## DISCUSSION

*CLCN7*-related ARO is a rare genetic bone disorder due to defects in bone resorption by osteoclasts. Investigations of the pathomechanisms of ARO are important for determining the molecular effects of individual mutations as well as for providing guidance for therapeutic strategies. Although these experiments are mostly performed in mouse models, the results from these animal model experiments can often not be extrapolated to humans. Besides, the use of animal models is increasingly criticized for ethical reasons. As an alternative approach, primary patient-derived cells can be used; however, the access to biopsy material is usually limited. For osteopetrosis, PBMC-derived osteoclasts provide a good model, but the quality of blood samples is often compromised due to prolonged transport and storage. In addition, only a limited number of experiments can be performed as *in vitro* expansion of these primary cells is not feasible.

Several osteoclast differentiation protocols from hiPSCs have been published. In 2009, Choi et al.<sup>(26)</sup> differentiated human ESCs and iPSCs using time-consuming techniques as Percoll gradient centrifugation and cell selection by surface marker expression for progenitor enrichment. Grigoriadis et al.<sup>(15)</sup> described a protocol utilizing five different differentiation media including up to seven cytokines and supplements. More recently, Jeon et al.<sup>(13)</sup> developed a more simplified osteoclast differentiation method based on only three media and in total three different cytokines. However, the efficiency of the osteoclast differentiation or the number of produced monocytes were not specified, but appeared rather low. In 2017, Chen et al.<sup>(12)</sup> presented their osteoclast differentiation protocol, which includes only one single monocyte harvesting step and required up to six cytokines and supplement additives in four differentiation media. Finally, Cui et al.<sup>(11)</sup> published a differentiation approach in 2019 using three different differentiation media based on expensive STEM-diff APEL 2 medium supplemented with up to eight cytokines and small molecules. Furthermore, the protocol does not include a monocyte production step, lasts up to 5 weeks, and the differentiation efficiency of 1.5% is low. By contrast, the osteoclast differentiation technique described here allows the continuous harvesting of monocyte-like cells over at least 9 weeks. We only use three differentiation media supplemented with only three or two cytokines and first osteoclasts emerged already after 4 weeks. The resulting osteoclast density of 41% on average and up to 73% in some experiments is very high.

Our in-depth characterization by flow cytometry, qRT-PCR, and expression profiling showed mesodermal induction in the first step, monocyte-like cell production in the second step,

and the generation of macrophages and osteoclasts in the final, third differentiation step. Terminally differentiated osteoclasts obtained by this procedure were multinucleated and displayed the characteristic podosome belt necessary for the sealing zone formation and thus the resorption process.<sup>(27)</sup>

The crucial criterion for successful osteoclast formation is bone resorption activity. Both, pits and trenches were generated by hiPSC-derived osteoclasts on dentine as well as on bovine cortical bone. Osteoclasts from BIHi004-A hiPSCs showed significantly more trenches than those from BIHi001-A and PBMCs; however, a large variability between different iPSC lines and their capacity to differentiate into specific cell types has been reported.<sup>(28)</sup> It has been demonstrated that osteoclasts making trenches reflect a more effective way of bone resorption.<sup>(19,29)</sup> Because we find that the proportion of trenches made by hiPSC-derived osteoclasts is equal or higher than for PBMCs-derived osteoclasts this highlights that iPSC-derived osteoclasts are effective at performing bone resorption. It has been shown that 67% of the variation in trenches between different osteoclast donors can be explained by the protein levels of activated cathepsin K.<sup>(30)</sup> Although we did not observe large differences in *CTSK* expression at messenger RNA (mRNA) level between PBMC-derived and hiPSC-derived osteoclasts, higher protein levels of activated cathepsin K in the latter could be a possible explanation. Moreover, it was clearly demonstrated that the level of multinucleation strongly facilitates trench-making osteoclasts, but not those that make pits. This is in line with our observation, because the increased fusion of hiPSC-derived osteoclasts correlated with a higher proportion of trenches. Recent studies suggest this might be linked to the expression of Dendritic cell-specific transmembrane protein (DC-STAMP).<sup>(31)</sup> However, the only gene known to be involved in osteoclast fusion more highly expressed in hiPSC-derived osteoclasts is *CCL2*. Again, this does not exclude differences in protein levels not correlating with mRNA levels.

To a large extent, osteoclasts derived from hiPSC lines tended to generate more “pseudoresorption”, reflecting a superficial staining of the bone surface without cavitation. Thus, only mild demineralization has been switched on, but collagenolysis apparently has not. We recently described a similar behavior of *LRRK1*-deficient osteoclasts.<sup>(18)</sup> Since we observed that iPSC-derived osteoclasts often become larger than PBMC-derived osteoclasts, it is conceivable that the increased level of pseudoresorption of hiPSC-osteoclasts could be a secondary effect of very large osteoclasts having problems to polarize properly and/or to form a proper sealing zone. Interestingly, we observed that large osteoclasts generated from human HSCs showed both an enhanced resorptive activity, but also increased levels of pseudoresorption (Hennig, unpublished observations). Because hiPSC-derived osteoclasts share these characteristics with osteoclasts differentiated from HSCs, but not with PBMC-derived osteoclasts, this hints at a difference in the maturation of these cells. This phenomenon is mirrored by the production of CD34<sup>+</sup> HSC-like cells during the first days of monocyte production. In addition, although typical osteoclast marker genes such as *CTSK* were expressed at equal levels in hiPSC-osteoclasts and PBMC-osteoclasts, hiPSC-osteoclasts showed higher levels of macrophage marker genes such as *MAF* and *CSF1R*, which can be interpreted as a sign of lower maturation of these cells. It is not unusual that hiPSC-derived cells are less mature than their primary counterparts. For example, cardiomyocytes derived from hiPSCs first show characteristics typical for fetal cardiomyocytes, although the hiPSCs were generated from adult cells.<sup>(32)</sup>

To demonstrate the usability of our osteoclast differentiation protocol for functional investigations, we applied it to the patient-derived osteopetrotic hiPSC line BIHi002-A.<sup>(16)</sup> The donor was diagnosed with ARO by a chest x-ray at the age of 7 months. Before this, the failure to thrive and neurological symptoms beginning at 4 months of age were interpreted as signs of a mitochondriopathy or a lysosomal storage disease. The MRI images of the central nervous system are highly reminiscent of a case with *OSTM1* mutations described by Maranda et al.<sup>(33)</sup> Also in this case, heterotopias and global cortical atrophy were observed. Similar to our case, this patient started to have seizures at 4 months of age and died at 1 year of age. In humans as well as in mice, (“grey lethal” mutants) *OSTM1* deficiency leads to a more severe brain phenotype than loss of *CLCN7*. It is currently unknown whether the *OSTM1*-ARO developmental brain phenotype is solely due to lysosomal dysfunction because a role of this protein in cytoskeletal organization and Wnt-signaling was also discussed.<sup>(34,35)</sup> The formation of enlarged osteoclasts with enhanced multinucleation is also a typical feature of osteoclasts with both *CLCN7* and *OSTM1* deficiency.<sup>(36,37)</sup> As a possible explanation, Pata and Vacher<sup>(36)</sup> discussed the dysregulation of the calcium and NFATc1 pathway and an indirect compensation mechanism due to the resorption inability in their *Ostm1*-knockout mouse. Neutzky-Wulff et al.<sup>(37)</sup> proposed that the absence of apoptotic factors normally released during the resorption process may expand lifespan and fusion of CIC-7 deficient osteoclasts. In the light of the overlap of the cellular and clinical phenotype of *OSTM1*-deficient and *CLCN7*-deficient mouse mutants and human patients, we suggest that the main pathomechanism in both cases is primarily a defective lysosomal ion homeostasis. Possibly, an early onset of severe lysosomal perturbation during postnatal brain maturation might affect neuronal migration leading to the observed heterotopias. *OSTM1* needs to bind to CIC-7 to exit the endoplasmic reticulum and for correct targeting.<sup>(21,38)</sup> Although we found that overexpressed CIC-7 harboring the mutations p.(G292E) or p.(R403Q) delivers *OSTM1* to the lysosome, *OSTM1* surface expression was barely detectable upon co-expression with plasma membrane-localized mutant CIC-7 (data not shown). If *OSTM1* would play a role independent of CIC-7, the remaining and correctly targeted *OSTM1* should be sufficient to prevent the phenotype, which is not the case.

The brain abnormalities of our patient appeared disproportionately severe compared to the degree of osteosclerosis and tardive bone marrow failure. The mutation p.(R403Q) was described in combination with the mutation p.(G521R) in another patient with global brain atrophy.<sup>(24)</sup> Because a heterozygous *CLCN7* gain-of-function mutation leading to increased lysosomal acidification and swelling was recently described that caused an exceptional neurological phenotype without bone involvement, we tested for the electrophysiological properties of the mutated CIC-7.<sup>(9)</sup> Although the severe amino acid exchange p.(G292E) completely abolished function, currents elicited by p.(R403Q) were changed in quantity (13% of WT levels), but not in quality. Because we previously found in transgenic experiments that 25% to 30% residual CIC-7 expression is needed for full cellular functionality, we assume that the overall reduced CIC-7 protein levels and the reduced currents for p.(R403Q) are far below this threshold.<sup>(39)</sup>

To address the possible role of abnormal lysosome functionality in the observed phenotypes we investigated the lysosomal pH. Lysosomal pH remained unchanged in osteopetrotic hiPSCs, and these findings correlate with previous investigations in

mouse fibroblasts, neurons, and macrophages from *Clcn7*-knockout mice.<sup>(4,40)</sup> The reason for the unchanged lysosomal pH is still unclear and controversially discussed. It has been shown that other cation channels support lysosomal acidification and CIC-7 is not essential.<sup>(7,40)</sup> However, CIC-7 probably regulates lysosomal function through intraluminal chloride concentrations and impacts lysosomal ion homeostasis in general.<sup>(41–43)</sup> However, we further investigated autophagy in ARO hiPSCs, because Wartosch et al.<sup>(6)</sup> and Weinert et al.<sup>(44)</sup> reported accumulation of the autophagy marker LC3-II in *Clcn7*-deficient murine tissues. Under normal culture conditions we observed similarly elevated levels of the autophagy marker LC3-II and an increase in the autophagic flux. Under starvation, however, this difference vanished, implying similar autophagy levels at maximum stimulation. Enhanced LC3-II levels might be due to a reduced turnover of autophagosomes, as the intra-autophagosomal LC3-II is only degraded by lysosomal proteases after fusion of the autophagosome with the lysosome and it was proposed that proteins are degraded with slower kinetics in CIC-7 knockout cells.<sup>(45)</sup> Interestingly, perturbed autophagy is the basis for several neurodevelopmental disorders.<sup>(46)</sup>

In future studies, poorly understood aspects of the osteopetrotic phenotype like the enlarged osteoclasts, the unchanged lysosomal pH or the defective autophagic flux could be molecularly dissected using engineered hiPSCs. Moreover, therapeutic approaches, including the research for novel targeted therapies, could be pursued in osteopetrotic hiPSC lines like the one presented here. Our novel differentiation protocol also might prove valuable for in vitro disease modeling of other osteoclast-related pathologies.

## ACKNOWLEDGMENTS

This project was part of the BCRT crossfield project GenoPro and was supported by the Berlin Institute of Health (BIH) through a BIH translational PhD grant to Uwe Kornak and Zsuzsanna Izsvák. This work was supported by the German Federal Ministry of Education and Research/German Center for Cardiovascular Research (to Lukas Cyganek), and by the German Research Foundation (SFB1002 S01 to Lukas Cyganek). This work was partly funded by the funding program of the academic grants committee of the Charité – Universitätsmedizin Berlin. Support was also provided by the Helmholtz Association through program-oriented funding and by the Federal Ministry of Education and Research, Germany, in the Programme HealthResearch (BCRT grant no. 13GW0098 and 13GW0099) and the European Community's Seventh Framework Programme under grant agreement no. 602300 (SYBIL) to Uwe Kornak. We thank Frank Konietschke and Asanka Gunawardana for their statistical advice and multiple helpful discussions. We are grateful to the BIH Core Facility Stem Cells for helpful advice and technical assistance regarding hiPSCs. We thank Jean-Marie Delaissé for inspiring discussions on osteoclasts and the initiation of a fruitful collaboration. We thank Jacob Bastholm Olesen for excellent technical assistance with the resorption analysis. We are grateful to Nico Lachmann and his team for their helpful advice regarding the initial steps of the hematopoietic differentiation process. Many thanks to Katriina Aalto-Setälä from Tampere University for providing one of the used induced pluripotent stem cell lines. The authors thank the UMG Stem Cell Unit for excellent technical support. The antibody H4A3 developed by August, J.T. / Hildreth, J.E.K. was

obtained from the Developmental Studies Hybridoma Bank, created by the NICHD of the NIH and maintained at The University of Iowa, Department of Biology, Iowa City, IA 52242. Open Access funding enabled and organized by Projekt DEAL.

Author contributions: Study design: Uta Rössler, Anna Floriane Hennig, Zsuzsanna Izsvák, Uwe Kornak. Study conduct: Uta Rössler, Anna Floriane Hennig, Uwe Kornak. Data collection: Uta Rössler, Anna Floriane Hennig, Nina Stelzer, Shroddha Bose, Johannes Kopp, Lukas Cyganek, Giovanni Zifarelli, Salaheddine Ali, Maja von der Hagen, Elisabeth Strässler, Gabriele Hahn. Data analysis: Uta Rössler, Anna Floriane Hennig, Shroddha Bose, Johannes Kopp, Kent Søre, Lukas Cyganek, Giovanni Zifarelli, Salaheddine Ali, Maja von der Hagen, Tobias Stauber, Uwe Kornak. Data interpretation: Uta Rössler, Anna Floriane Hennig, Kent Søre, Lukas Cyganek, Michael Pusch, Tobias Stauber, Manfred Gossen, Harald Stachelscheid, Uwe Kornak. Writing manuscript: Uta Rössler, Anna Floriane Hennig, Uwe Kornak. Revising manuscript content: Uta Rössler, Anna Floriane Hennig, Kent Søre, Lukas Cyganek, Tobias Stauber, Zsuzsanna Izsvák, Manfred Gossen, Harald Stachelscheid, Uwe Kornak. Approving final version of manuscript: all authors; The following individuals take responsibility for the integrity of the data analysis: Uta Rössler, Anna Floriane Hennig, Uwe Kornak.

## DISCLOSURES

The authors report no conflict of interest.

## PEER REVIEW

The peer review history for this article is available at <https://publons.com/publon/10.1002/jbmr.4322>.

## DATA AVAILABILITY STATEMENT

Data are available upon request.

## REFERENCES

1. Sobacchi C, Schulz A, Coxon FP, Villa A, Helfrich MH. Osteopetrosis: genetics, treatment and new insights into osteoclast function. *Nat Rev Endocrinol*. 2013;9(9):522-536.
2. Supancharit C, Kornak U. Ion channels and transporters in osteoclasts. *Arch Biochem Biophys*. 2008;473(2):161-165.
3. Chalhoub N, Benachenhou N, Rajapurohitam V, et al. Grey-lethal mutation induces severe malignant autosomal recessive osteopetrosis in mouse and human. *Nat Med*. 2003;9(4):399-406.
4. Kasper D, Planells-Cases R, Fuhrmann JC, et al. Loss of the chloride channel CIC-7 leads to lysosomal storage disease and neurodegeneration. *EMBO J*. 2005;24(5):1079-1091.
5. Kornak U, Kasper D, Bösl MR, et al. Loss of the CIC-7 chloride channel leads to osteopetrosis in mice and man. *Cell*. 2001;104(2):205-215.
6. Wartosch L, Fuhrmann JC, Schweizer M, Stauber T, Jentsch TJ. Lysosomal degradation of endocytosed proteins depends on the chloride transport protein CIC-7. *FASEB J*. 2009;23(12):4056-4068.
7. Weinert S, Jabs S, Supancharit C, et al. Lysosomal pathology and osteopetrosis upon loss of H<sup>+</sup>-driven lysosomal Cl<sup>-</sup> accumulation. *Science*. 2010;328(5984):1401-1403.
8. Ott CE, Fischer B, Schröter P, et al. Severe neuronopathic autosomal recessive osteopetrosis due to homozygous deletions affecting OSTM1. *Bone*. 2013;55(2):292-297.
9. Nicolini ER, Weston MR, Hackbarth M, et al. Lysosomal storage and albinism due to effects of a De Novo CLCN7 variant on lysosomal acidification. *Am J Hum Genet*. 2019;104(6):1127-1138.
10. Lachmann N, Ackermann M, Frenzel E, et al. Large-scale hematopoietic differentiation of human induced pluripotent stem cells provides granulocytes or macrophages for cell replacement therapies. *Stem Cell Rep*. 2015;4(2):282-296.
11. Cui X, Cui Y, Shi L, Luan J, Zhou X, Han J. A preliminary study on the mechanism of skeletal abnormalities in Turner syndrome using inducing pluripotent stem cells (iPS)-based disease models. *Intractable Rare Dis Res*. 2019;8(2):113-119.
12. Chen IP, Luxmi R, Kanaujija J, Hao Z, Reichenberger EJ. Craniometaphyseal dysplasia mutations in ANKH negatively affect human induced pluripotent stem cell differentiation into osteoclasts. *Stem Cell Rep*. 2017;9(5):1369-1376.
13. Jeon OH, Panicker LM, Lu Q, Chae JJ, Feldman RA, Elisseff JH. Human iPSC-derived osteoblasts and osteoclasts together promote bone regeneration in 3D biomaterials. *Sci Rep*. 2016;6:26761.
14. Neri T, Muggeo S, Paulis M, et al. Targeted gene correction in osteopetrosis-induced pluripotent stem cells for the generation of functional osteoclasts. *Stem Cell Rep*. 2015;5(4):558-568.
15. Grigoriadis AE, Kennedy M, Bozoc A, et al. Directed differentiation of hematopoietic precursors and functional osteoclasts from human ES and iPSC cells. *Blood*. 2010;115(14):2769-2776.
16. Hennig AF, Rössler U, Boiti F, et al. Generation of a human induced pluripotent stem cell line (BIHi002-A) from a patient with CLCN7-related infantile malignant autosomal recessive osteopetrosis. *Stem Cell Res*. 2019;35:101367.
17. Buchrieser J, James W, Moore MD. Human induced pluripotent stem cell-derived macrophages share ontogeny with MYB-independent tissue-resident macrophages. *Stem Cell Rep*. 2017;8(2):334-345.
18. Howaldt A, Hennig AF, Rolvien T, et al. Adult osteosclerotic metaphyseal dysplasia with progressive osteonecrosis of the jaws and abnormal bone resorption pattern due to a LRRK1 splice site mutation. *J Bone Miner Res*. 2020;35(7):1322-1332.
19. Merrild DM, Pirapaharan DC, Andreasen CM, et al. Pit- and trench-forming osteoclasts: a distinction that matters. *Bone Res*. 2015;3:15032.
20. Leisle L, Ludwig CF, Wagner FA, Jentsch TJ, Stauber T. CIC-7 is a slowly voltage-gated 2Cl<sup>-</sup>/1H<sup>+</sup>-exchanger and requires Ostm1 for transport activity. *EMBO J*. 2011;30(11):2140-2152.
21. Stauber T, Jentsch TJ. Sorting motifs of the endosomal/lysosomal CLC chloride transporters. *J Biol Chem*. 2010;285(45):34537-34548.
22. Klionsky DJ, Abdelmohsen K, Abe A, et al. Guidelines for the use and interpretation of assays for monitoring autophagy (3rd edition). *Autophagy*. 2016;12(1):1-222.
23. Takayanagi H. Osteoimmunology: shared mechanisms and crosstalk between the immune and bone systems. *Nat Rev Immunol*. 2007;7(4):292-304.
24. Pangrazio A, Pusch M, Caldana E, et al. Molecular and clinical heterogeneity in CLCN7-dependent osteopetrosis: report of 20 novel mutations. *Hum Mutat*. 2010;31(1):E1071-E1080.
25. Phadke SR, Fischer B, Gupta N, Ranganath P, Kabra M, Kornak U. Novel mutations in Indian patients with autosomal recessive infantile malignant osteopetrosis. *Indian J Med Res*. 2010;131:508-514.
26. Choi KD, Vodyanik MA, Slukvin II. Generation of mature human myelomonocytic cells through expansion and differentiation of pluripotent stem cell-derived lin<sup>-</sup>CD34<sup>+</sup>CD43<sup>+</sup>CD45<sup>+</sup> progenitors. *J Clin Invest*. 2009;119(9):2818-2829.
27. Teitelbaum SL. The osteoclast and its unique cytoskeleton. *Ann NY Acad Sci*. 2011;1240:14-17.
28. Ortmann D, Vallier L. Variability of human pluripotent stem cell lines. *Curr Opin Genet Dev*. 2017;46:179-185.
29. Søre K, Delaissé JM. Time-lapse reveals that osteoclasts can move across the bone surface while resorbing. *J Cell Sci*. 2017;130(12):2026-2035.
30. Borggaard XG, Pirapaharan DC, Delaissé JM, Søre K. Osteoclasts' ability to generate trenches rather than pits depends on high levels of active cathepsin K and efficient clearance of resorption products. *Int J Mol Sci*. 2020;21(16):5924.
31. Møller AMJ, Delaissé JM, Olesen JB, et al. Fusion potential of human osteoclasts in vitro reflects age, menopause, and in vivo bone



- resorption levels of their donors-A possible involvement of DC-STAMP. *Int J Mol Sci.* 2020;21(17):6368.
32. Bellin M, Marchetto MC, Gage FH, Mummery CL. Induced pluripotent stem cells: the new patient? *Nat Rev Mol Cell Biol.* 2012;13(11):713-726.
  33. Maranda B, Chabot G, Décarie JC, et al. Clinical and cellular manifestations of OSTM1-related infantile osteopetrosis. *J Bone Miner Res.* 2008;23(2):296-300.
  34. Feigin ME, Malbon CC. OSTM1 regulates beta-catenin/Lef1 interaction and is required for Wnt/beta-catenin signaling. *Cell Signal.* 2008;20(5):949-957.
  35. Pandruvada SN, Beauregard J, Benjannet S, et al. Role of Ostm1 cytosolic complex with kinesin 5B in intracellular dispersion and trafficking. *Mol Cell Biol.* 2015;36(3):507-521.
  36. Pata M, Vacher J. Ostm1 bifunctional roles in osteoclast maturation: insights from a mouse model mimicking a human OSTM1 mutation. *J Bone Miner Res.* 2018;33(5):888-898.
  37. Neutzsky-Wulff AV, Sims NA, Supanchart C, et al. Severe developmental bone phenotype in CIC-7 deficient mice. *Dev Biol.* 2010;344(2):1001-1010.
  38. Lange PF, Wartosch L, Jentsch TJ, Fuhrmann JC. CIC-7 requires Ostm1 as a beta-subunit to support bone resorption and lysosomal function. *Nature.* 2006;440(7081):220-223.
  39. Supanchart C, Wartosch L, Schlack C, et al. CIC-7 expression levels critically regulate bone turnover, but not gastric acid secretion. *Bone.* 2014;58:92-102.
  40. Steinberg BE, Huynh KK, Brodovitch A, et al. A cation counterflux supports lysosomal acidification. *J Cell Biol.* 2010;189(7):1171-1186.
  41. Zifarelli G. A tale of two CLCs: biophysical insights toward understanding CIC-5 and CIC-7 function in endosomes and lysosomes. *J Physiol.* 2015;593(18):4139-4150.
  42. Stauber T, Jentsch TJ. Chloride in vesicular trafficking and function. *Annu Rev Physiol.* 2013;75:453-477.
  43. Astaburuaga R, Quintanar Haro OD, Stauber T, Relógio A. A mathematical model of lysosomal ion homeostasis points to differential effects of Cl<sup>-</sup> transport in Ca<sup>2+</sup> dynamics. *Cell.* 2019;8(10):1263.
  44. Weinert S, Jabs S, Hohensee S, Chan WL, Kornak U, Jentsch TJ. Transport activity and presence of CIC-7/Ostm1 complex account for different cellular functions. *EMBO Rep.* 2014;15(7):784-791.
  45. Wartosch L, Stauber T. A role for chloride transport in lysosomal protein degradation. *Autophagy.* 2010;6(1):158-159.
  46. Teinert J, Behne R, Wimmer M, Ebrahimi-Fakhari D. Novel insights into the clinical and molecular spectrum of congenital disorders of autophagy. *J Inherit Metab Dis.* 2020;43(1):51-62.